

PAPER

The compressed breast during mammography and breast tomosynthesis: *in vivo* shape characterization and modeling

To cite this article: Alejandro Rodríguez-Ruiz *et al* 2017 *Phys. Med. Biol.* **62** 6920

View the [article online](#) for updates and enhancements.


Related content

- [Dosimetry in x-ray-based breast imaging](#)
David R Dance and Ioannis Sechopoulos
- [A scatter correction method for contrast-enhanced dual-energy digital breast tomosynthesis](#)
Yihuan Lu, Boyu Peng, Beverly A Lau *et al.*
- [Estimation of scattered radiation in digital breast tomosynthesis](#)
O Diaz, D R Dance, K C Young *et al.*

Recent citations

- [Internal breast dosimetry in mammography: Monte Carlo validation in homogeneous and anthropomorphic breast phantoms with a clinical mammography system](#)
Christian Fedon *et al*

The compressed breast during mammography and breast tomosynthesis: *in vivo* shape characterization and modeling

Alejandro Rodríguez-Ruiz¹ , Greeshma A Agasthya²
and Ioannis Sechopoulos^{1,3}

¹ Department of Radiology and Nuclear Medicine, Radboud University Medical Centre, Geert Grooteplein 10, 6525 GA, Nijmegen, Netherlands

² Department of Radiology and Imaging Sciences, Emory University, 1364 Clifton Road NE, Atlanta, GA 30322, United States of America

³ Dutch Reference Centre for Screening (LRCB), Wijchenseweg 101, 6538 SW, Nijmegen, Netherlands

E-mail: Ioannis.Sechopoulos@radboudumc.nl

Received 26 April 2017, revised 9 June 2017

Accepted for publication 30 June 2017

Published 7 August 2017



CrossMark

Abstract

To characterize and develop a patient-based 3D model of the compressed breast undergoing mammography and breast tomosynthesis.

During this IRB-approved, HIPAA-compliant study, 50 women were recruited to undergo 3D breast surface imaging with structured light (SL) during breast compression, along with simultaneous acquisition of a tomosynthesis image. A pair of SL systems were used to acquire 3D surface images by projecting 24 different patterns onto the compressed breast and capturing their reflection off the breast surface in approximately 12–16 s. The 3D surface was characterized and modeled via principal component analysis. The resulting surface model was combined with a previously developed 2D model of projected compressed breast shapes to generate a full 3D model.

Data from ten patients were discarded due to technical problems during image acquisition. The maximum breast thickness (found at the chest-wall) had an average value of 56 mm, and decreased 13% towards the nipple (breast tilt angle of 5.2°). The portion of the breast not in contact with the compression paddle or the support table extended on average 17 mm, 18% of the chest-wall to nipple distance. The outermost point along the breast surface lies below the midline of the total thickness. A complete 3D model of compressed breast shapes was created and implemented as a software application available for

download, capable of generating new random realistic 3D shapes of breasts undergoing compression.

Accurate characterization and modeling of the breast curvature and shape was achieved and will be used for various image processing and clinical tasks.

Keywords: breast modeling, breast tomosynthesis, mammography, structured light, compressed breast shape

 Supplementary material for this article is available [online](#)

(Some figures may appear in colour only in the online journal)

1. Introduction

Digital mammography (DM) and digital breast tomosynthesis (DBT) require mechanical breast compression during image acquisition. Several areas of research in DM and DBT, such as scatter correction (Sechopoulos *et al* 2007b, Feng and Sechopoulos 2011, Diaz *et al* 2014, Feng *et al* 2014) and thickness correction (Snoeren and Karssemeijer 2004, Kallenberg and Karssemeijer 2012) algorithms, require simulating realistic 3D compressed breast shapes (some approaches for scatter correction such as the one proposed by Kim *et al* (2015) do not require this). Moreover, other areas of research like patient dosimetry (Dance 1990, Dance *et al* 2000, Sechopoulos *et al* 2007a, 2012), breast density estimation (Gubern-Merida *et al* 2014, Pertuz *et al* 2016), image registration and segmentation (Richard *et al* 2006, Hipwell *et al* 2016), and 3D breast software phantoms (Bakic *et al* 2002, 2011, Wang *et al* 2012, Hsu *et al* 2013, O'Connor *et al* 2013, Kiarashi *et al* 2015) could also benefit from objective shape models of compressed breasts to improve their accuracy and relevance.

Until now, most of this research uses simplistic compressed breast models both in 2D and 3D. For example, 2D projections are reduced to a semi-elliptical approximation for the cranio-caudal (CC) mammography view (Dance 1990, Boone and Cooper 2000) or a subjective model for the medio-lateral oblique (MLO) view (Sechopoulos *et al* 2007a). Also, the 3D curvature of the compressed breast is also usually modeled as a semicircle (Snoeren and Karssemeijer 2004, Kallenberg and Karssemeijer 2012) or as an arbitrary polynomial (Feng *et al* 2014). In our previous work (Feng *et al* 2013, Rodríguez-Ruiz *et al* 2017) we developed a 2D model of the projection of the outer shape of compressed breasts in digital mammograms, based on the objective analysis of a previously acquired database of mammograms. Now, we include for the first time the detailed characterization and modeling of the 3D compressed breast tissue curvature between the support table and the compression paddle. This is accomplished by directly imaging patients' breast surface with state-of-the-art structured light (SL) technology. SL cameras are widely used to register static surfaces in an ample diversity of fields, such as plant phenotyping (Nguyen *et al* 2016), authentication of paintings (Buchón-Moragues *et al* 2016), or for planning of allotransplantations (Mäkitie *et al* 2016). Moreover, this technology can achieve more than 10 times the resolution of DBT to characterize breast surfaces. The DBT limited angular sampling results in a limited in-depth resolution, ranging between 2 and 5 mm across systems (Rodríguez-Ruiz *et al* 2016a, 2016b). To facilitate the applicability of the model, which is based on direct measurements of patients' compressed breast shapes, we develop a software tool able to generate random realistic 3D shapes representative of a breast during compression for DM and DBT image acquisition.

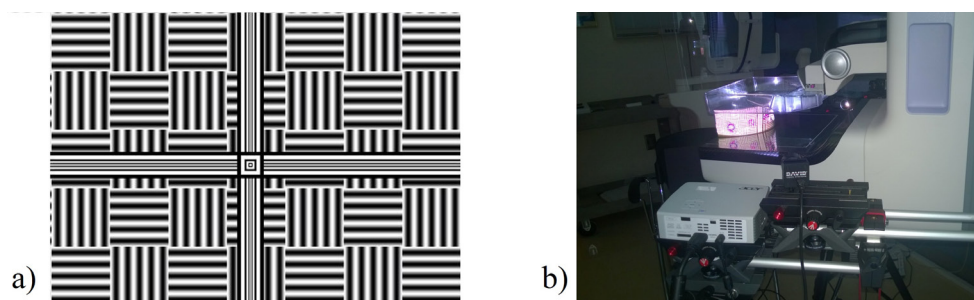


Figure 1. (a) Example pattern projected by the system during acquisition and (b) photograph of SL scanning system.

2. Materials and methods

2.1. Study population

During this IRB-approved, HIPAA-compliant study, 50 women presenting at the Emory University Breast Imaging Center between October 2014 and March 2015 for breast cancer screening were recruited after undergoing informed consent. They were consecutively enrolled and the only exclusion criteria was previous history of mastectomy or lumpectomy.

2.2. Protocol and imaging techniques

The images of the breast surface were acquired with two sets of SL scanning systems. SL scanning combines a digital projector (K132, Acer Inc, Xizhi, New Taipei, Taiwan) that projects 24 different patterns such as the one shown in figure 1(a) onto the object of interest, with a digital camera (USB CMOS Monochrome Camera 3.1-M, David Visions Systems, Palo Alto, CA, USA) that captures the reflection of these patterns. Acquisition of the entire series of patterns takes approximately 6–8 s. The accuracy of these scans was previously tested with phantoms of known thickness (Model 082, CIRS, Norfolk, VA, USA) and was found to be 0.3 mm (Agasthya and Sechopoulos 2015).

After acquisition, computer software (DAVID-3 software, David Visions Systems) processes the set of images to create a 3D representation of the surface of the scanned object. Since this technology works with normal light, no radiation dose is involved, and no laser light is used, requiring no eye protection. Two SL scanning systems were used to increase the breast coverage. The sets were mounted on tripods and placed to the left and right side of the DM/DBT unit (figure 1(b)). The lateral sides of the compression paddle were covered with a thin opaque tape to avoid reflections and distortions in the images, hence this did not affect the normal clinical scenario.

The patient's breast was positioned on the support paddle and compressed as usual for acquisition of a clinical CC-view DBT image. Afterwards, the two compressed 3D breast surface images were consecutively acquired, for a total scan time of 12–16 s. In parallel to 3D surface image acquisition, a DBT CC view of the breast was acquired with a Selenia Dimensions system (Hologic Inc., Bedford, MA, USA) in 3–4 s. By acquiring DBT simultaneously, patient movement between acquisitions was minimized.

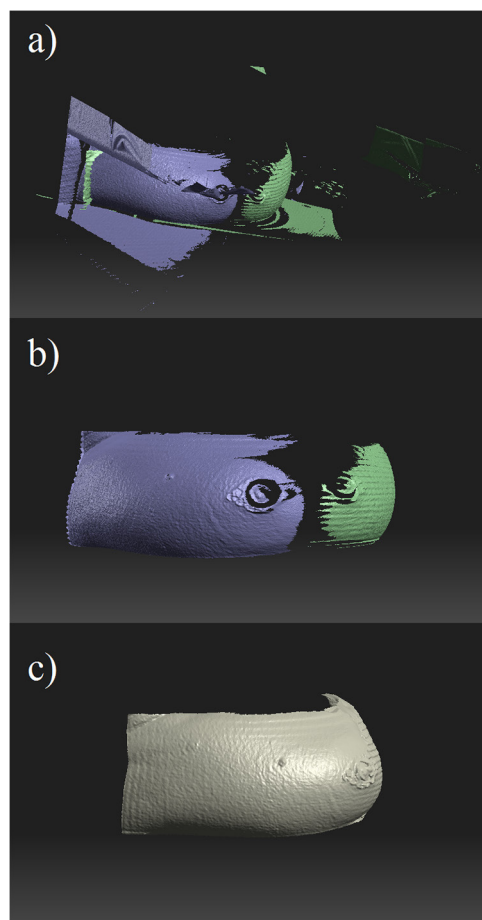


Figure 2. Post processing of the 3D external breast surface: (a) raw surface images acquired by the two scanning cameras, (b) the signals that do not belong to the breast surface are removed; and (c) images from both lateral cameras are fused using a registration tool available in the software by the manufacturer, called global fine registration.

2.3. Post processing of the breast 3D surface

The raw images (figure 2(a)) from both 3D scanning cameras were first processed and fused. Any signal not corresponding to the breast surface, such as from the compression paddle or the support table, was removed (figure 2(b)). Then, the medial and lateral scans of the same breast were aligned and fused using global fine registration (figure 2(c)). These processes were done manually using the DAVID-3 software.

2.4. 3D characterization of the compressed breast surface: arcs

The breast surface between the compression paddle and the support table from each patient was characterized with a set of 13 (chosen to characterize the breast every 15°) equiangular-spaced arcs. For this, as seen from the top, the breast was considered as a semi-circular object centered at the mid-point along the chest-wall (figure 3(a)). From this center point, rays were

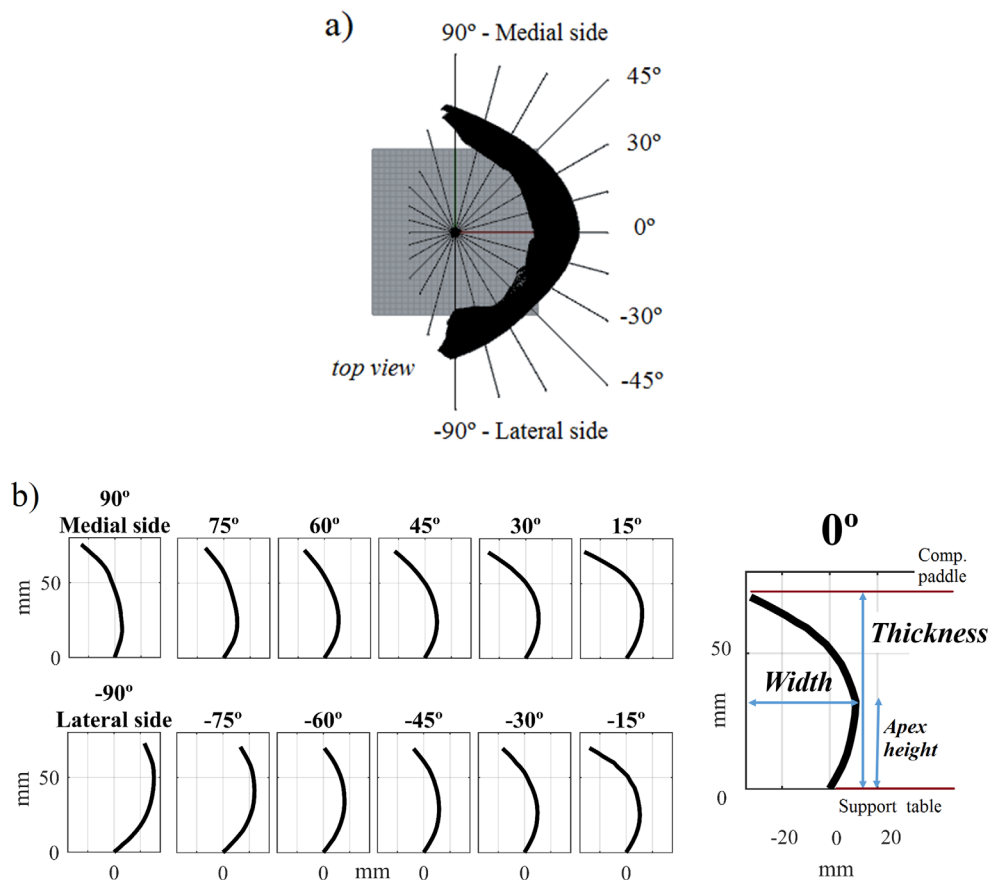


Figure 3. Example of the characterization of the breast surface displayed in figure 2 with arcs. (a) Semi-automated process of extracting 13 equiangular spaced radial arcs of the breast surface every 15°, and (b) the final result after post-processing the arcs to remove inhomogeneities and artifacts.

cast out every 15° and their intersection with the breast surface defined the location of these 13 arcs, from +90° (medial side) to -90° (lateral side), where 0° describes approximately the nipple location (figure 3(a)). This processing was semi-automatically performed with a script implemented in Rhinoceros 5 (McNeel North America, Seattle, WA, USA).

Arcs were post-processed with a script in Matlab 2016a (MathWorks, Natick, MA, USA) to remove noise and the nipple, when present. Noise in the arcs was removed with a moving average smoothing filter. The nipple was detected and removed using a previously described procedure (Rodríguez-Ruiz *et al* 2017). Briefly, larger than average changes in the gradient of the arc curve are detected using a running standard deviation of the gradient along the arc points, by identifying deviations that go beyond three times the average level. In this way, once detected, the points of the arc belonging to the nipple contour can be delimited, and then replaced by a second order polynomial extrapolated from the rest of points of the arc. Finally, each arc was resampled to 20 equispaced coordinate points (figure 3(b)).

Arcs instead of the whole surface mesh were chosen to represent the breast surface in order to simplify its posterior characterization and modeling, especially considering limited amount of patient data.

2.5. Comparison of breast tissue coverage between imaging modalities

To determine the effectiveness of the surface scans in covering the entire compressed breast, three breast dimensions were estimated from the surface scans and compared to those obtained from the central DBT projection acquired simultaneously. Paired t-tests were used to compare the metrics between imaging modalities.

2.5.1. SL image-calculated breast dimensions. First, the maximum thickness of the 3D breast surface, found on the chest wall, was calculated and denote the SL breast thickness (Th_{SL}). Also, the maximum distance between the center point of the breast and the most anterior point of the breast surface was computed and denoted the SL chest-wall to nipple distance (CND_{SL}). Then the largest area enclosed by the breast surface, considering the outermost perimeter, was computed and denoted the SL area (A_{SL}).

2.5.2. Breast tomosynthesis image-calculated breast dimensions. From the central DBT projection, the thickness was retrieved from the DICOM header (Th_{DBT}). The chest-wall to nipple distance (CND_{DBT}) was calculated as the maximum distance between the chest-wall edge of the image and the most anterior point of the breast. Finally, the breast area (A_{DBT}) was computed by automatically detecting the outer edge of the breast image and calculating the enclosed area, as previously described (Rodríguez-Ruiz *et al* 2017). The CND_{DBT} and A_{DBT} were corrected for magnification (Ren *et al* 2005), assuming that the projected image was generated from the center of the total breast thickness.

2.6. Analysis of the characteristics of the compressed breast external surface

The thickness, width, and height of the apex (the outermost point along the height of the breast) of each arc was calculated to study possible dependencies along the breast contour (figure 3(b)). The difference between the maximum and minimum thickness among arcs was also computed to obtain the tilt angle of the top surface of the compressed breast between the chest-wall and the nipple.

2.7. Principal component analysis (PCA) of the breast surface arcs

PCA of the arcs was performed with two different datasets as inputs, in order to represent the breast surface with both a basic and a more advanced model. For the basic model, the same curvature was assumed for the entire breast contour, hence it only modeled one arc. The dataset for the basic model was composed only of arcs extracted at $\pm 45^\circ$ from each breast shape (after visual inspection, found to be a good approximation of the average external surface along the compressed breast). The arcs from each side ($\pm 45^\circ$) were considered independent and thus the number of samples for the basic model is twice the number of patients included. The advanced model involved all 13 arcs from each breast (from $+90^\circ$ to -90° , as described above).

2.71. Principal component analysis. Following the same procedure as detailed previously (Feng *et al* 2013, Rodríguez-Ruiz *et al* 2017), the set of arcs can be reduced to a smaller set of linearly independent parameters via PCA, comprising most of the information present in the data points (Jolliffe 2002). Based on the PCA results, histograms were computed of the first twelve (found to be enough to represent the breast surface in detail) PCA model parameter values of all studied breasts. These histograms were fit with a Gaussian distribution (mean μ , standard deviation σ) to generate new random arcs representing realistic objective model-based breast surfaces. The exact influence of each parameter j on the shape of the arcs was studied after varying its value independently, from $(\mu_j - 2\sigma_j)$ to $(\mu_j + 2\sigma_j)$, while the other parameters were held constant at their mean values.

2.72. Testing the basic model to represent arcs not used in the PCA. The ability of the basic PCA model to characterize arcs with a small set of parameters was tested by leave-one-out cross validation (Kearns and Ron 1999). For this, the PCA model was built repeatedly using all but one of the total k arcs available, varying which j arc was excluded from the set each time. For each of these k iterations, the j arc was modeled with the PCA built with the other $k - 1$ arcs (Feng *et al* 2013, Rodríguez-Ruiz *et al* 2017). The similarity between the modeled (j_m) and the original arc (j) was tested with the discrete Fréchet distance.

The Fréchet distance is a wide-spread measure of the similarity between two curves. Eiter and Mannila (1994) presented in their work the discrete Fréchet distance δ_{dF} which is a good approximation of the continuous variable. Since our curves (arcs) are depicted by a limited fixed number of points, 20, the discrete approximation that considers curves as polygonal chains is appropriate for our purpose. Therefore, δ_{dF} represents the maximum distance between two corresponding points among the entire sets of points depicting the modeled edge (j_m) and the original edge (j). This analysis was repeated for different number of PCA parameters, to determine how many were needed to obtain an adequate model.

2.8. Objective 3D model of compressed breast shapes

An objective full 3D model of compressed breast shapes was created from the *in vivo* characterization of the patients breast shape. This model combines the PCA of the arcs and the 2D projected outer breast shape model from mammograms reported previously (Rodríguez-Ruiz *et al* 2017). The only overlap between Rodríguez-Ruiz *et al* (2017) and this paper is the use of some of the segmentation methods and the PCA methodology, as described above.

The 3D model was implemented on a Matlab GUI application, available for download as supplementary material (stacks.iop.org/PMB/62/6920/mmedia) and explained in appendix. With this application, the user can generate clinical relevant shapes of compressed breasts undergoing acquisition of CC view DM and DBT images. The 2D model and the model of the arcs were combined in a sequential procedure described in appendix, which also depicts how the software tool works.

3. Results

3.1. Study population

The mean age of the patients included in the study was 59 years (range 42–76). Post-processing of the breast surfaces revealed that the surface scans of 10 patients (20%) had low image quality and were discarded. The main differences between the composition of the included

Table 1. Characteristics of the patients and the imaged breast shapes. Where applicable, mean values, and standard deviations within parentheses, are shown. BI-RADS® breast density assessment was extracted from the clinical report. Thickness was retrieved from the DICOM header.

	Overall (<i>n</i> = 50)	Included (<i>n</i> = 40)	Excluded (<i>n</i> = 10)
Age (<i>y</i>)	59 (9)	59 (9)	56 (10)
Race	Caucasian: 38 Non-caucasian: 12	C: 32 N-C: 8	C: 6 N-C: 4
Imaged breast laterality	Left: 25 Right: 25	L: 19 R: 21	L: 6 R: 4
Breast density (BI-RADS®)	<i>a</i> : 12 <i>b</i> : 19 <i>c</i> : 18 <i>d</i> : 1	<i>a</i> : 8 <i>b</i> : 15 <i>c</i> : 16 <i>d</i> : 1	<i>a</i> : 4 <i>b</i> : 4 <i>c</i> : 2 <i>d</i> : 0
Force (<i>N</i>)	98 (28)	97 (26)	102 (30)
Thickness (mm)	61.7 (13.3)	59.2 (11.8)	71.7 (14.3)

Table 2. Comparison of breast tissue coverage metrics between DBT and SL 3D surface cameras. Mean values and standard deviations within parentheses are shown. Thickness on the central DBT projection was retrieved from the DICOM header.

	Area (cm ²)	CND (mm)	Thickness (mm)
Central DBT projection	150 (58)	103 (26)	59.2 (11.8)
SL 3D cameras	145 (53)	97 (22)	56.2 (13.0)
<i>p</i> -value	0.09	0.03	<0.001

and excluded groups were race and breast thickness. 33% of all the non-Caucasian women enrolled in the study had to be discarded, while 16% of Caucasians were discarded. Regarding compressed breast thickness, excluded patients had breasts that were thicker by an average of 21% than those of included patients (71.7 mm, range 59.5–81.5 mm; versus 59.1 mm, range 51.0–68.5 mm; $p < 0.05$). Full characteristics of the enrolled, included and excluded population can be found in table 1.

3.2. Comparison of breast tissue coverage between imaging modalities

Table 2 shows the average values of thickness, chest-wall to nipple distance and area measured by the SL 3D cameras and by DBT, while figure 4 shows scatter plots comparing the values for each of these measurements per patient.

3.3. Analysis of the characteristics of the compressed breast external surface

As expected, it was found that breast thickness decreases towards the nipple direction, on average by 13% (standard deviation $\pm 5\%$) of the height at the chest-wall (figure 5), where 13.2 mm was the largest decrease found among patients. The medial side ($+90^\circ$ direction) was 4.5 ± 2.9 mm thicker than at 0° . The lateral side (-90° direction) was on average 2.7 ± 3.4 mm thicker than at 0° , and statistically different than the thickness on the medial side ($p < 0.05$). The breast thickness as function of radial position along the breast surface can be fit to a second order polynomial ($R^2 = 0.99$), with a minimum value at approximately -10° (figure 5).

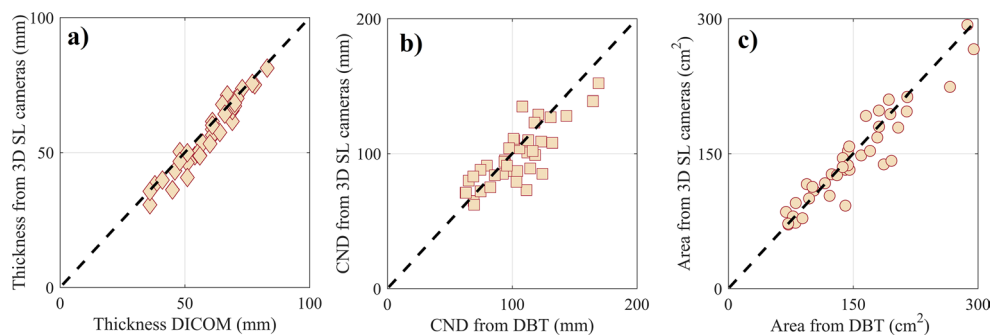


Figure 4. Scatter plots comparing the (a) thickness, (b) chest-wall to nipple distance and (c) area of the imaged breasts computed from the DBT images and the SL 3D camera images per patient. The dashed lines represent identity.

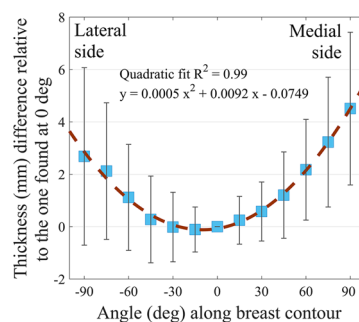


Figure 5. Average thickness difference along the breast surface relative to the thickness at the central radial position (0°). 90° indicates the medial side of the compressed breast, and -90° corresponds to the lateral side. Error bars represent the \pm standard deviation.

Averaged across all arcs of all breasts, the thickness was 51.6 ± 12.7 mm (-13% difference versus DICOM-reported thickness).

The ratio apex height/total breast thickness showed higher values for the lateral side (0.55 versus 0.43 on the medial side, figure 6). Averaged along the breast surface, the relative apex height was 0.41 ± 0.11 , significantly lower than 0.5 ($p < 0.001$). This means that, on average, the most anterior portion of the compressed breast is below the mid-height line (figure 7).

No clear relationship was found between the width of the arcs (figure 3(b)) and their angular position along the breast surface. Only slightly larger widths on the nipple, medial and lateral sides were found. The mean curvature width averaged across arcs was 17 ± 9 mm, which corresponds to 18% of the average CND_{SL} (figure 7). No relationship was found between either arc width and CND_{SL} or A_{SL} .

Considering an average CND_{SL} of 97 mm, all the above mentioned results correspond to an average compressed breast tilt angle of 5.2° (figure 7). This value agrees ($p = 0.3$) with the average breast tilt angle found across our population, 4.9° (CI 95%: 4.2 – 5.2°). Also, the points of contact with the breast support plate and compression paddle are not at the same location. At the compression paddle the breast is on average 6 mm recessed than at the breast support plate (figure 7).

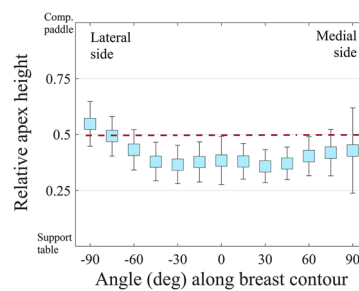


Figure 6. Relative height of the apex as function of position along the breast surface. 90° indicates the medial side of the compressed breast, and -90° corresponds to the lateral side. Error bars represent the \pm standard deviation.

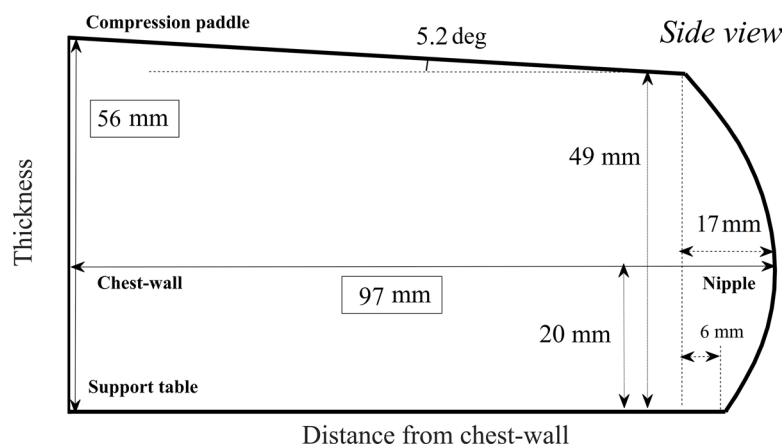


Figure 7. Dimensions of the average compressed breast undergoing DM and DBT, based on the breast surface images from 40 patients. Diagram not to scale.

3.4. PCA of the arcs: basic and advanced modeling

To include 99% of the cumulative variance encountered in the patient data, the three first principal components of the simple model are needed, while the first ten of the advanced model are needed. However, using the first four components of the advanced model encompasses 95% of the cumulative patient variance.

Using the basic model, the discrete Fréchet distance between the modeled and original arcs is shown in table 3, as a function of the number of components included in the PCA model. As expected, there is a consistent improvement in representing the arc shape more accurately with an increasing number of components, showing both lower mean values and lower values for the standard deviation. Examples of the discrete Fréchet distance can be found in figure 8.

The mean arcs from both models are displayed in figure 9. It was found that for both models, the first principal component (alpha) has a strong linear relationship ($R^2 > 0.96$) with breast thickness (figure A2). The other components define finer details of breast curvature (figure A3). Since not all parameters are normally distributed in the models, only the first 6 components are considered for the random generation of new arcs.

Table 3. Discrete Fréchet distance (δ_{dF}) obtained during leave-one-out cross validation of the basic PCA model, as a function of the number of components used in the model. The standard deviation is shown in parentheses. The δ_{dF} was computed between the modeled and original arc excluded from the leave-one-out PCA model.

	Number of components of the basic model					
	2	3	4	5	6	7
δ_{dF} (mm)	1.7 (1.4)	0.5 (0.3)	0.4 (0.2)	0.3 (0.2)	0.3 (0.2)	0.2 (0.1)

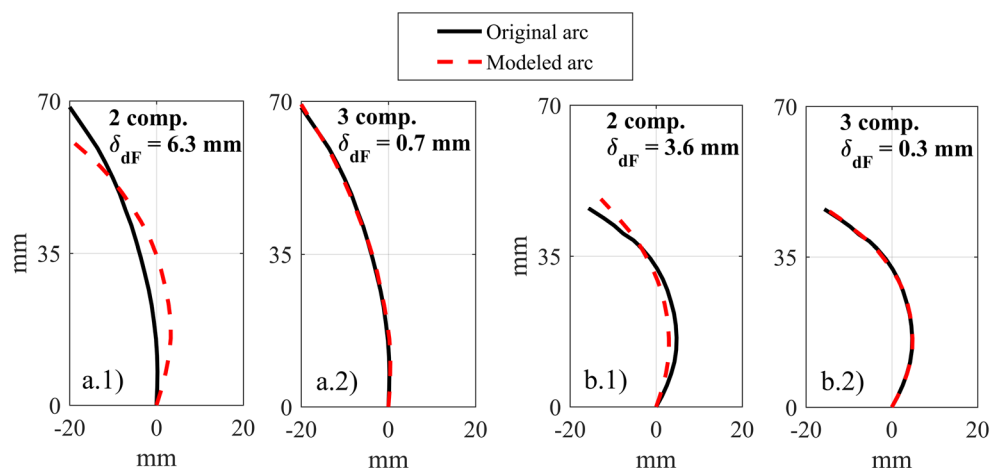


Figure 8. Two examples of the discrete Fréchet distance between the original and modeled arcs for different number of components used in the PCA model.

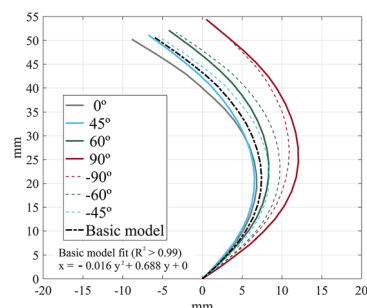


Figure 9. Mean arcs from the advanced model at different angles along the breast surface (90° medial side, to -90° lateral side), and mean curvature arc of the basic model (built from samples at $\pm 45^\circ$).

4. Discussion

A 3D model of compressed breast shapes is developed based on patient images acquired with a new SL 3D surface imaging technique. The main application of our models is the generation of new random compressed breast shapes. The basic model could be useful for applications where there is no need for fine detail, for example, the simulation of x-ray scatter, which is a low-frequency signal. The basic model does not include a reduction in thickness

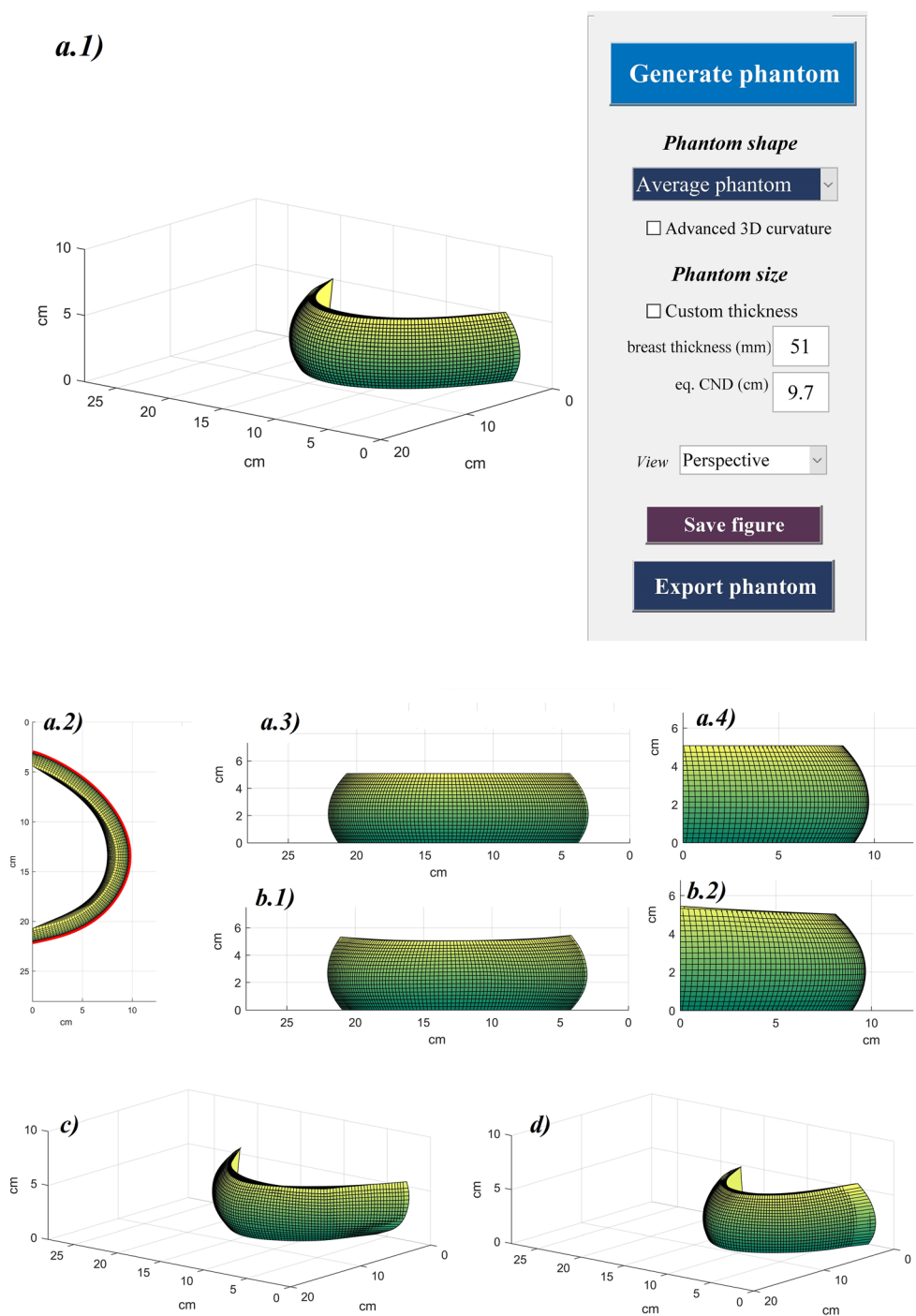


Figure A1. Examples of the application to generate the full 3D model of compressed breast shapes undergoing mammography or breast tomosynthesis. (a.1)–(a.4) Different views of the average breast shape generated with the basic model which assumes a constant curvature along the surface. (b.1) and (b.2) Average breast shape generated with the advanced model which assumes a varying curvature along the surface. (c) and (d) Examples of randomly generated compressed breast shapes with the advanced model.

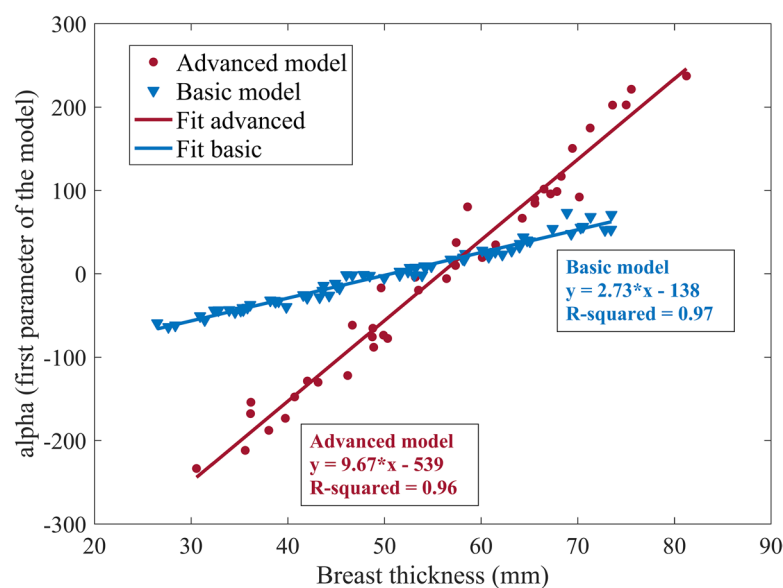


Figure A2. First principal component of both models, alpha, as a function of breast thickness computed with the 3D cameras. In both cases, there is a linear relationship ($R^2 > 0.96$) that can be used to customize the thickness of new random breast shapes.

from the chest wall to the nipple or varying curvature along the breast surface, as opposed to the advanced model. However, it still provides significantly better accuracy than a surface directly reconstructed from a DBT scan. The advanced model could be used for breast modeling research, to complement models with high internal complexity that might benefit a more accurate external breast shape.

The decrease in breast thickness from the chest-wall to the anterior of the breast found here is similar to results from other authors (Mawdsley *et al* 2009, Tyson *et al* 2009). The average minimum thickness was found slightly displaced towards the lateral side (-10° , with respect to the central radial position). This might be caused by the nipple, also reported to be displaced towards the lateral side in our previous work (Rodríguez-Ruiz *et al* 2017). Thickness from SL cameras is slightly smaller than DICOM-reported thickness, but we have to consider that we did not measure it directly on the center of the breast at the chest-wall. There is moderate agreement on breast tissue coverage between SL cameras and DBT images, so this could be expected.

The average CND_{DBT} measured in this work is comparable but slightly smaller to the 12.4 cm reported by Broeders *et al* (2015). The average compressed breast tilt angle in the chest-wall to nipple direction is slightly larger than the 1.3° tilt reported by Snoeren and Karssemeijer (2004) with an indirect measurement, but it lies within the range of 0° – 8.53° directly measured by Mawdsley *et al* (2009).

The relative height of the outermost point of the compressed breast is below the mid-line of the breast curvature (statistically significant lower than 0.5), perhaps due to gravity (figure 7). The number of patients scanned in this study is too low to determine if the shape of the arc of breast tissue between compression paddle and support plate varies with age and/or glandular density. It could be expected that more glandular breasts are less affected by gravity, even during compression, than more adipose breasts. Furthermore, this ratio was almost

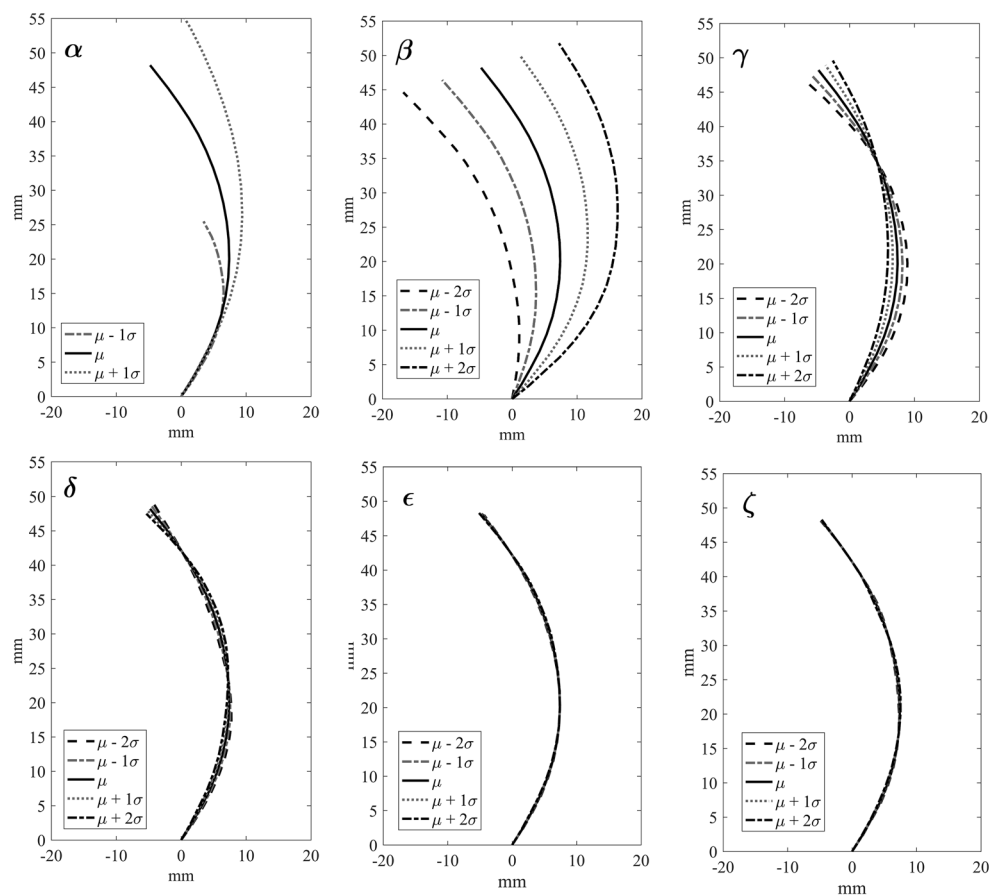


Figure A3. Arcs generated by varying the first six PCA parameters of the basic model individually. Each parameter was set to the mean value (μ) found across our population, as well as to $\mu \pm$ one standard deviation (σ) and $\mu \pm 2\sigma$ (except for alpha, where we only chose $\pm 1\sigma$ to avoid going beyond the observed range of alpha parameters in our dataset). Similar behavior is found for the advanced model.

0.6 on the lateral side, maybe indicating that the breast is not as free to move posteriorly as it is anteriorly. The analysis of discrete Fréchet distances showed that our model can be used to accurately (<1 mm) represent new imaged arcs with a low number of linearly independent parameters.

This study has allowed us to detect possible drawbacks of this new imaging technique, which need to be addressed in the future. In general, we have found that both the breast support table and the compression paddle of the mammography system are prone to distort the signal of the projectors due to reflections. These artifacts could easily be avoided by covering these elements with, for example, opaque tape. Since this tape is only on the lateral sides (directly facing the SL cameras), is easy to integrate in the clinical setting. Also, because the pattern lines are black, darker skin made the surface imaging more challenging. In our study, the scanning time of the SL cameras was greater than that of the DBT acquisition (12–16 s versus 3–4 s), however, it has to be considered that scan time of some DBT systems is over 20 s. In addition, further optimization of the hardware and software of the SL cameras could

lower the acquisition time of the SL images. Therefore, the use of SL cameras does not necessarily lengthen the patient workflow.

Moreover, we have also experienced poor image coverage for thicker breasts, as the excluded patients have thicker breasts than the included population. This coverage limitation is mainly due to hardware resources. A recent update from the manufacturer allows to scan with three or four cameras while still using only two projectors, hence the total scan time would not increase, but this could allow for enhanced angular coverage, which was the main limiting factor when having to discard some data due to lack of overlap in coverage. As a consequence we expect that the 20% failure rate found in this pilot study will significantly decrease in future studies with updated hardware.

Another limitation of this work is that only the CC view was studied. Capturing these surface images during MLO view compressions will require a more complex camera setup that needs to be further investigated in the future. Also, the full automation of the post-processing of the raw 3D surface images is something to be addressed, especially if a larger number of patients is to be studied. Finally, the inclusion of only 50 patients and only one mammography manufacturer could introduce a limitation in the generalizability of the results. However, it is not expected that the characterization of the breast shape would vary considerably when compressed by different mammography systems.

5. Conclusion

With this project we developed a patient-based 3D model of compressed breast shapes undergoing mammography and breast tomosynthesis. This imaging technique allows, for the first time, to accurately characterize the breast under compression. In addition to obtaining information for breast modeling, this methodology could be used during mammography or breast tomosynthesis acquisition for improved image processing and/or reconstruction, as well as other clinical tasks, such as breast volumetric estimation and registration (Fradkin *et al* 2013, Howes *et al* 2014, Chae *et al* 2016), 3D printing of realistic phantoms, and aiding in the planning of breast surgery.

Acknowledgments

Supported in part by Grant No. R01CA163746 and Grant No. R01CA181171 from the National Cancer Institute, National Institutes of Health and Grant No. IIR13262248 from the Susan G Komen Foundation for the Cure.

Appendix. Functioning of the 3D model

Both the basic and the advanced 3D models described in this manuscript can be used with the application available for download with this publication (see supplementary material at stacks.iop.org/PMB/62/6920/mmedia for the necessary software to use the developed models). The GUI of the application that implements the objective 3D model of compressed breast shapes is displayed on figure A1.

The 2D model (Rodríguez-Ruiz *et al* 2017) and the model of the arcs were combined in a sequential procedure described below, which also depicts how the software tool works.

- (1) User selects whether to generate an average or random compressed breast shape and whether to use the basic or advanced breast curvature arc model.

- (2) A 2D breast mammography projection image (random or average) is created with the 2D model. The area A of this projection is computed and corrected for magnification. The magnification factor considers an air gap of 2.5 cm between the breast support table and the detector surface (Ren *et al* 2005), and it assumes the projection area was generated from the center of the total breast thickness.
- (3) This area is then associated with a DICOM-reported breast thickness following figure 4 in our previous work (Rodríguez-Ruiz *et al* 2017). A Gaussian random factor with a variance of 8 mm accounts for the data dispersion.
- (4) This DICOM thickness value is then corrected by an offset in relation to the actual thickness measured by the surface cameras.
- (5) The corrected thickness can be related to the first parameter of the curvature model (figure A2).
- (6) The other PCA parameters of the breast curvature model are computed randomly (following the observed distribution of PCA parameters in our population) or the average is taken (depending on step 1). They define finer details of breast curvature (figure A3)
- (7) With all the generated PCA parameters, a new set of arcs representing a breast surface can be computed.
- (8) From these arcs, the complete 3D shape of the breast surface is built at each point of the 2D projection by interpolation. This 2D projection is assumed to be at the height of apex of each arc.

ORCID iDs

Alejandro Rodríguez-Ruiz  <https://orcid.org/0000-0002-7554-5561>

References

- Agasthya G and Sechopoulos I 2015 TU-CD-207-09: analysis of the 3D shape of patients' breast for breast imaging and surgery planning *Med. Phys.* **42** 3612
- Bakic P R, Albert M, Brzakovic D and Maidment A D 2002 Mammogram synthesis using a 3D simulation. I. Breast tissue model and image acquisition simulation *Med. Phys.* **29** 2131–9
- Bakic P R, Zhang C and Maidment A D 2011 Development and characterization of an anthropomorphic breast software phantom based upon region-growing algorithm *Med. Phys.* **38** 3165–76
- Boone J M and Cooper V N III 2000 Scatter/primary in mammography: Monte Carlo validation *Med. Phys.* **27** 1818–31
- Broeders M J *et al* 2015 Comparison of a flexible versus a rigid breast compression paddle: pain experience, projected breast area, radiation dose and technical image quality *Eur. Radiol.* **25** 821–9
- Buchón-Moragues F, Bravo J M, Ferri M, Redondo J and Sánchez-Pérez J V 2016 Application of structured light system technique for authentication of wooden panel paintings *Sensors* **16** 881
- Chae M P, Rozen W M, Spychal R T and Hunter-Smith D J 2016 Breast volumetric analysis for aesthetic planning in breast reconstruction: a literature review of techniques *Gland Surg.* **5** 212
- Dance D R 1990 Monte Carlo calculation of conversion factors for the estimation of mean glandular breast dose *Phys. Med. Biol.* **35** 1211–9
- Dance D R, Skinner C L, Young K C, Beckett J R and Kotre C J 2000 Additional factors for the estimation of mean glandular breast dose using the UK mammography dosimetry protocol *Phys. Med. Biol.* **45** 3225–40
- Diaz O, Dance D R, Young K C, Elangovan P, Bakic P R and Wells K 2014 Estimation of scattered radiation in digital breast tomosynthesis *Phys. Med. Biol.* **59** 4375–90

- Eiter T and Mannila H 1994 Computing discrete fréchet distance *Report* CD-TR 94/64, Technical University of Vienna
- Feng S S J, D'Orsi C J, Newell M S, Seidel R L, Patel B and Sechopoulos I 2014 X-ray scatter correction in breast tomosynthesis with a precomputed scatter map library *Med. Phys.* **41** 031912
- Feng S S J, Patel B and Sechopoulos I 2013 Objective models of compressed breast shapes undergoing mammography *Med. Phys.* **40** 031902
- Feng S S J and Sechopoulos I 2011 A software-based x-ray scatter correction method for breast tomosynthesis *Med. Phys.* **38** 6643–53
- Fradkin M, Hofmann M C, Rouet J-M, Moore R H, Kopans D B, Tipton K, Suryanarayanan S, Boas D A and Fang Q 2013 Diagnosing breast cancer using independent diffuse optical tomography and x-ray mammography scans *Proc. SPIE 8574, Multimodal Biomedical Imaging VIII* p 85740G
- Gubern-Merida A, Kallenberg M, Platel B, Mann R M, Marti R and Karssemeijer N 2014 Volumetric breast density estimation from full-field digital mammograms: a validation study *PLoS One* **9** e85952
- Hipwell J H, Vavourakis V, Han L, Mertzaniidou T, Eiben B and Hawkes D J 2016 A review of biomechanically informed breast image registration *Phys. Med. Biol.* **61** R1–31
- Howes B H, Fosh B, Watson D I, Yip J M, Eaton M, Smallman A and Dean N R 2014 Autologous fat grafting for whole breast reconstruction *Plastic Reconstr. Surg. Glob. Open* **2** e124
- Hsu C M, Palmeri M L, Segars W P, Veress A I and Dobbins J T III 2013 Generation of a suite of 3D computer-generated breast phantoms from a limited set of human subject data *Med. Phys.* **40** 043703
- Jolliffe I T 2002 *Principal Component Analysis* (New York: Springer)
- Kallenberg M G and Karssemeijer N 2012 Compression paddle tilt correction in full-field digital mammograms *Phys. Med. Biol.* **57** 703–15
- Kearns M and Ron D 1999 Algorithmic stability and sanity-check bounds for leave-one-out cross-validation *Neural Comput.* **11** 1427–53
- Kiarashi N, Nolte A C, Sturgeon G M, Segars W P, Ghate S V, Nolte L W, Samei E and Lo J Y 2015 Development of realistic physical breast phantoms matched to virtual breast phantoms based on human subject data *Med. Phys.* **42** 4116–26
- Kim K *et al* 2015 Fully iterative scatter corrected digital breast tomosynthesis using GPU-based fast Monte Carlo simulation and composition ratio update *Med. Phys.* **42** 5342–55
- Mäkitie A, Salmi M, Lindford A, Tuomi J and Lassus P 2016 Three-dimensional printing for restoration of the donor face: a new digital technique tested and used in the first facial allotransplantation patient in Finland *J. Plast. Reconstr. Aesthet. Surg.* **69** 1648–52
- Mawdsley G E, Tyson A H, Peressotti C L, Jong R A and Yaffe M J 2009 Accurate estimation of compressed breast thickness in mammography *Med. Phys.* **36** 577–86
- Nguyen T T, Slaughter D C, Maloof J N and Sinha N 2016 Plant phenotyping using multi-view stereo vision with structured lights *Proc. SPIE 9866, Autonomous Air and Ground Sensing Systems for Agricultural Optimization and Phenotyping* pp 986608–9
- O'Connor J M, Das M, Dider C S, Mahd M and Glick S J 2013 Generation of voxelized breast phantoms from surgical mastectomy specimens *Med. Phys.* **40** 041915
- Pertuz S, McDonald E S, Weinstein S P, Conant E F and Kontos D 2016 Fully automated quantitative estimation of volumetric breast density from digital breast tomosynthesis images: preliminary results and comparison with digital mammography and MR imaging *Radiology* **279** 65–74
- Ren B, Ruth C, Stein J, Smith A, Shaw I and Jing Z 2005 Design and performance of the prototype full field breast tomosynthesis system with selenium based flat panel detector *Medical Imaging* (International Society for Optics and Photonics) pp 550–61
- Richard F J, Bakic P R and Maidment A D 2006 Mammogram registration: a phantom-based evaluation of compressed breast thickness variation effects *IEEE Trans. Med. Imaging* **25** 188–97
- Rodríguez-Ruiz A, Castillo M, Garayoa J and Chevalier M 2016a Evaluation of the technical performance of three different commercial digital breast tomosynthesis systems in the clinical environment *Phys. Med.* **32** 767–77

- Rodríguez-Ruiz A, Castillo M, Garayoa J and Chevalier M 2016b Further results on the evaluation of the performance of a digital breast tomosynthesis system in the clinical environment *Phys. Med.* **32** 217
- Rodríguez-Ruiz A, Feng S S, van Zelst J, Vreemann S, Rice Mann J, D'Orsi C J and Sechopoulos I 2017 Improvements of an objective model of compressed breasts undergoing mammography: generation and characterization of breast shapes *Med. Phys.* **44** 2161–72
- Sechopoulos I, Bliznakova K, Qin X, Fei B and Feng S S 2012 Characterization of the homogeneous tissue mixture approximation in breast imaging dosimetry *Med. Phys.* **39** 5050–9
- Sechopoulos I, Suryanarayanan S, Vedantham S, D'Orsi C J and Karellas A 2007a Computation of the glandular radiation dose in digital tomosynthesis of the breast *Med. Phys.* **34** 221–32
- Sechopoulos I, Suryanarayanan S, Vedantham S, D'Orsi C J and Karellas A 2007b Scatter radiation in digital tomosynthesis of the breast *Med. Phys.* **34** 564–76
- Snoeren P R and Karssemeijer N 2004 Thickness correction of mammographic images by means of a global parameter model of the compressed breast *IEEE Trans. Med. Imaging* **23** 799–806
- Tyson A H, Mawdsley G E and Yaffe M J 2009 Measurement of compressed breast thickness by optical stereoscopic photogrammetry *Med. Phys.* **36** 569–76
- Wang Y, Keller B M, Zheng Y, Acciavatti R J, Gee J C, Maidment A D and Kontos D 2012 A phantom study for assessing the effect of different digital detectors on mammographic texture features *Int. Workshop on Digital Mammography* (Berlin: Springer) pp 604–10